Biosensors and Bioelectronics 25 (2009) 418–427

Contents lists available at ScienceDirect

Biosensors and Bioelectronics

journal homepage: www.elsevier.com/locate/bios

In-vitro sensing of biomechanical forces in live cells by a whispering gallery mode biosensor

Michael Himmelhaus*, Alexandre Francois[1]

Fujirebio, Inc., Research and Development Division, 51 Komiya-cho, 192-0031, Hachioji-shi, Tokyo-to, Japan

ARTICLE INFO

Article history:
Received 13 May 2009
Received in revised form 9 July 2009
Accepted 27 July 2009
Available online 3 August 2009

Keywords:
Endocytosis
Biomechanics
Cortical tension
Whispering gallery modes
Cavity modes
Optical force sensor
Remote sensor
Biosensor

ABSTRACT

Direct measurement of the biomechanical stress induced by a live cell during endocytosis is reported. Fluorescent dye-doped polystyrene microspheres were used as microscopic remote optical sensors applying whispering gallery modes (WGMs) as transducer mechanism. Monitoring of the WGMs throughout the incorporation of the microsphere into the cell enabled the determination of the deformation experienced by the microsphere, characterized by both a broadening and a blue shift of the resonances, and consequently the stress induced by the cell. The results reveal an unexpectedly high stress with a magnitude of up to five times that of the passive cortical tension, which can be only explained by a so far undetermined active stress component induced by the cytoskeletal machinery during particle incorporation. The method is adaptable to the study of any other kind of phagocyte and thus provides a novel research tool of high interest for cell biology.

1. Introduction

Endothelial cells are known as "non-professional" phagocytes (Rabinovitch, 1995) with the ability to incorporate small particles by endocytosis (Porta et al., 1992; Wiewrodt et al., 2002). While the origin of this aptitude has not yet been fully understood, it seems to be related to the removal of apoptotic cells from (Hess et al., 1997; Kirsch et al., 2007) and the transmigration of leucocytes through the endothelial tissue (Feng et al., 1998; Cook-Mills and Deem, 2005; Hordijk, 2006; Vestweber, 2007), and thus contributes vividly to the body's inflammatory and immunological response. Both endocytosis and transcytosis are triggered by biochemical (Greenberg, 2001; Hordijk, 2006; Vestweber, 2007) and biomechanical (Cinamon et al., 2001; Herant et al., 2006) signals. While a lot of emphasis has been placed on the elucidation of biochemical signaling pathways, the function of mechanical forces is less understood (Herant et al., 2005; Herant et al., 2006), not least because they are more difficult to access experimentally. Nevertheless, it has been shown that endocytic pathways also address the actin and microtubule cytoskeleton (Garcia et al., 1998; Kielbassa et al., 1998; Apodaca, 2001). In the following, we introduce a novel microscopic remote sensor for in-vitro force measurements inside the cellular cortex by optical tracking of the mechanical deformation of a spherical probe during its endocytosis. As transducer mechanism, we apply whispering gallery mode (WGM) excitations in the fluorescent probe particle. In contrast to the most commonly utilized evanescent field coupling (Serpengüzel et al., 1995; Vahala, 2003; Matsko and Ilchenko, 2006; Vollmer and Arnold, 2008), this scheme for WGM excitation facilitates the use of small particles of only few microns in diameter and further supersedes any optomechanical coupling between the probe and its ambient, thus promoting undistorted real-time observation of the entire process of endocytosis. This direct and unvarnished access reveals a so far undetermined active stress component induced by the cytoskeletal machinery during particle incorporation with a magnitude of up to five times that of the passive cortical tension. The method is adaptable to the study of any other kind of phagocyte and thus provides a novel research tool of high interest for cell biology, inflammation and immunology, and cancer research, where mechanical phenotyping has recently been applied to cancer diagnosis (Remmerbach et al., 2009; Brunner et al., 2009).

2. Sensing principle

Experimentally, the cortical tension of different cell types has been determined to about 0.1 mN/m at rest (Wolfe et al., 1986) and up to 1 mN/m during endocytosis (Herant et al., 2006). This

* Corresponding author. Tel.: +81 42 645 4774; fax: +81 42 645 4758.
E-mail address: ml-himmelhaus@fujirebio.co.jp (M. Himmelhaus).
[1] Present address: Center for Photonics, Centre of Expertise in Photonics, School of Chemistry and Physics, The University of Adelaide, 5005, Australia.

0956-5663/$ – see front matter © 2009 Elsevier B.V. All rights reserved.
doi:10.1016/j.bios.2009.07.021

"passive" stress component, however, does not include active mechanical forces (Micoulet et al., 2005), e.g., mediated by molecular motors, by which the cell may pull the particle to force its incorporation, as recently postulated by Herant et al. (Herant et al., 2006). This "active" component, which operates assumedly directly between particle and cytoskeleton, has not yet been determined. We tackle this fundamental question here by implementing an optical transducer mechanism based on WGM excitations inside of a probe during its endocytosis, which thus acts in a kind of "stealth mode" not perceptible for the cell.

The WGMs' bandwidths and wavelength positions depend crucially on the probe's size and shape and thus provide precise information about its mechanical deformation in all three dimensions, thereby enabling the distinction of the different stress components as induced, e.g., by the cytoskeleton during endocytosis by active pulling of the phagosome (Herant et al., 2006). As illustrated in Fig. 1a, WGMs inside of a spherical dielectric particle travel in a plane along the particle/ambient interface by total internal reflection (Oraevsky, 2002). The modes can be described by their polarization[2] and three quantum numbers related to the number of field maxima in radial (q), azimuthal (ℓ), and polar ($\ell - m + 1 > 0$) directions. ℓ and m are angular quantum numbers, so that the $2\ell + 1$ polar modes are all degenerate, i.e., as long as spherical symmetry is preserved, the plane of mode propagation can be freely chosen (Fig. 1c). In the case of a mechanical deformation, however, degeneracy is lifted resulting in a band broadening (Fig. 1d) (Ilchenko et al., 1998; Kippenberg et al., 2005; Gerlach et al., 2007), from which the deformation can be calculated.

Tracking of deformations requires the excitation and detection of modes in all polar orientations (*cf.* Fig. 1d). We achieve this by exploiting fluorescent particles for WGM excitation (Kuwata-Gonokami et al., 1992; Weller et al., 2008) instead of the evanescent field coupling schemes mostly applied (Serpengüzel et al., 1995; Vahala, 2003; Matsko and Ilchenko, 2006; Vollmer and Arnold, 2008). Upon excitation by means of a focused laser beam, the dye emits arbitrarily in all directions, thereby populating all cavity modes available in its emission regime independent of their polar orientation. Because of the simplicity of this excitation scheme, WGMs can be successfully generated in much smaller particles than in the case of evanescent field coupling, which requires minute control of nanometer-sized gaps between microresonator and its optical coupler and thus puts much higher demands on the mechanical precision of the optomechanical set-up. Obviously, remote control of the microresonator is hampered under such conditions. In contrast, when applying the fluorescent WGM excitation scheme as performed in the following, WGM detection is simply mediated by spectral analysis of the fluorescence emission of the probe particle, thereby rendering the system into a fully radiation – and thus remotely – controlled optical sensor that may freely float in an aqueous medium. The present study became merely possible because of these three benefits of internal WGM excitation via fluorescence, which are (i) WGM excitation in three dimensions, (ii) excitation in particles sufficiently small to allow their endocytosis by live cells, and (iii) the opportunity for remote (radiation-controlled) operation of the system.

We apply polystyrene (PS) as sensor material because PS beads are available in the required size range with excellent sphericity and surface homogeneity, which is mandatory for the measurement of bead deformations. Further, its higher refractive index and lower E-modulus as compared to silica beads makes PS the material of choice for the measurement of bead deformations in an aqueous environment.

As cellular model system for endocytosis, we selected human umbilical vein endothelial cells (HUVECs) not only because of their biomedical significance, but also because particle incorporation proceeds on a much longer time scale (typically 100–120 min) than with professional phagocytes, which act typically within few minutes (Herant et al., 2006). The slower process helps to minimize a potential influence of the laser exposure and thus ensures an undistorted observation of the process of endocytosis in this primary study.

3. Materials and methods

3.1. Materials

PS microspheres with nominal diameters of 6–10 μm were purchased from Polysciences, Inc., Warrington, PA; poly(allylamine hydrochloride) (PAH), MW ~15,000 Da, poly(sodium 4 styrenesulfonate) (PSS), MW ~70,000 Da, 11-mercaptoundecanoic acid (MUA), and xylene, p.a. grade, were received from Sigma–Aldrich K. K., Tokyo, Japan; acetone and ethanol, both p.a. grade, were obtained from Wako Pure Chemical Industr. Ltd., Osaka, Japan; phosphate buffered saline (PBS) and Coumarin 6 laser grade (C6G) dye were purchased from MP Biomedicals, Solon, OH, and polydimethylsiloxane (Sylgard 184; PDMS) from Dow Corning Co., Midland, MI; all chemicals were used as received. Microscopy cover slips, $32 \times 24 \times 0.17\,mm^3$, were obtained from Matsunami Glass Industries, Ltd., Osaka, Japan; uncoated Sensor Au chips for SPR were purchased from Biacore K. K., Tokyo, Japan. DI water was produced with a Milli-Q system from Millipore, S.A., Molsheim, France, equipped with an automatic sanitization module.

HUVECs and endothelial cell growth medium (ECGM; basal ECGM cat. no. 210-485 and ECGM supplement cat. no. 211-GS) were purchased from Cell Applications, Inc., San Diego, CA, BD falcon 75 cm^2 cell culture flasks, cat. no. 430 725, from BD Biosciences, Bedford, MA, and Hanks balanced salt solution, 0.25% trypsin/1 mM EDTA 4Na solution, and trypsin neutralizing solution from invitrogen Japan K. K., Tokyo, Japan.

3.2. Methods

3.2.1. Microsphere sample preparation

PS microspheres were doped with C6G by using a liquid two-phase system. A saturated C6G/xylene solution was placed on top of a diluted microsphere suspension in de-ionized (DI) water and stirred until the xylene had completely evaporated. The suspension was then washed by centrifugation, removal of the supernatant and subsequent replacement of the lost volume by DI water. This rinsing step was repeated twice before coating the doped beads with two polyelectrolyte (PE) double layers of PAH/PSS following the layer-by-layer deposition method described elsewhere (see, e.g., Caruso et al., 1999). Microscope glass cover slips were coated with PAH/PSS layers similar to the routine described by Lösche et al. (Lösche et al., 1998) in order to promote adhesion of HUVECs. Then, the glass substrate was attached to a microfluidic flow cell made of PDMS and structured with a rectangular flow channel of $15 \times 2 \times 0.1\,mm^3$ in size. The channel was filled with ECGM and allowed to equilibrate for few hours prior to the injection of HUVECs.

3.2.2. Cell culturing

Cells were cultured in BD Falcon 75 cm^2 cell culture flasks according to the provider's instructions and in-house standard protocols, split and re-cultured to third passage (P-3). P-3 cells were

[2] TE: transverse electric field, TM: transverse magnetic field. Due to different boundary conditions for TE and TM fields at the resonator/ambient interface, WGMs for TE and TM show slight differences in the energy levels even for modes of same quantum numbers.

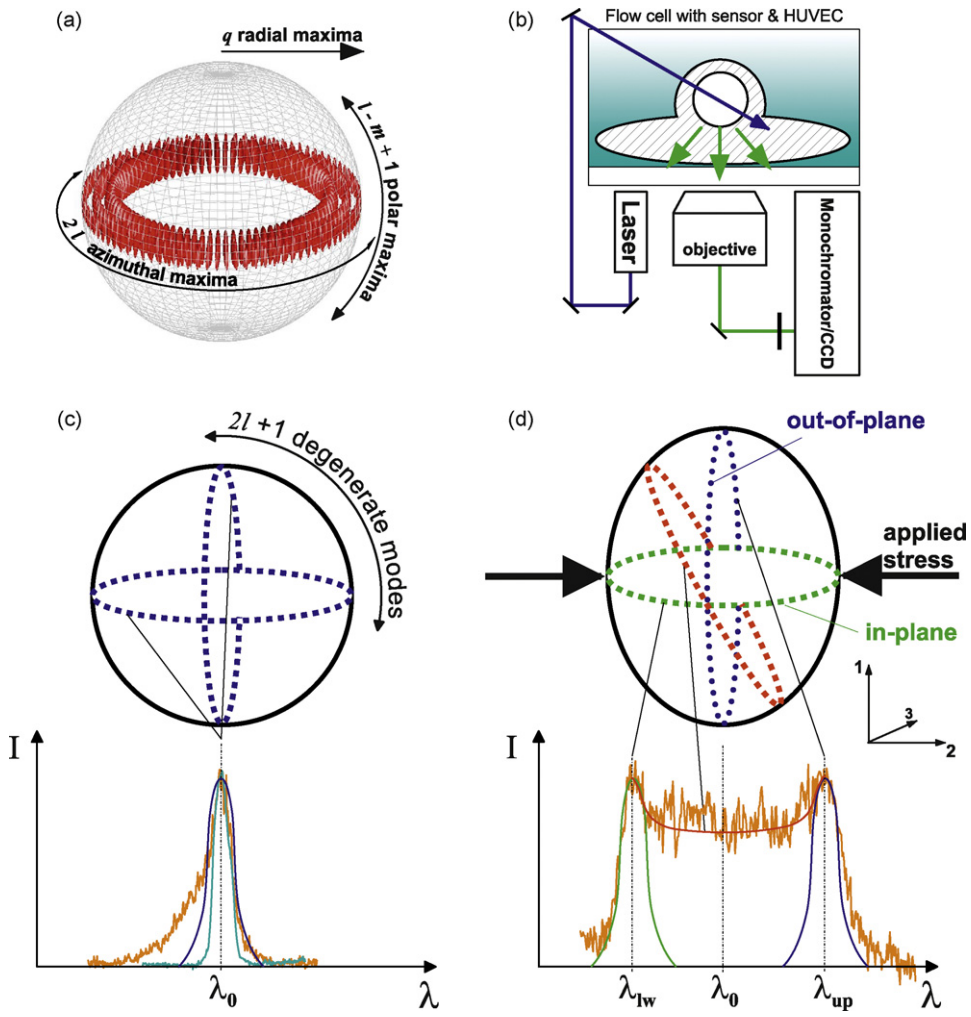

Fig. 1. Illustration of the sensing principle. (a) Graphical illustration of a whispering gallery mode (WGM) with quantum numbers $q = 3$ (radial), $\ell = 71$ (azimuthal), and $m = \ell$ (polar); (b) sketch of the experimental set-up (not drawn to scale); (c) WGMs degenerate in the polar quantum number m in a spherical bead. Besides a sketch of the expectedly symmetric mode (blue), the $TE_{\ell=71}$ mode of the $t = 0$ min spectrum of Fig. 3a (orange) and the $TE_{\ell=90}$ mode of the $t = 0$ spectrum of Fig. 3b (cyan) are shown to illustrate the asymmetry in the former case indicating bead-cell contact; (d) loss of degeneracy by deformation of the bead into an ellipsoid due to applied stress. The mode positions are now different for WGMs traveling in planes with different polar angles causing mode broadening into a band, whereby the outer boundaries show an enhancement due to the higher symmetry of the ellipsoid's principal axes, which in turn yields smaller bandwidths and thus higher quality factors, $Q = \lambda/\Delta\lambda$, for these extremes. The $TE_{\ell=71}$ peak of the $t = 5$ min spectrum of Fig. 3a is shown (orange) for illustration.

injected into the flow cell pre-filled with ECGM and incubated at 37° for about 4 h before the start of the experiment.

3.2.3. Bead uptake

Equilibrated beads were injected into the flow cell, in which HUVECs had been grown at sub-monolayer coverage. After injection, the flow was stopped to avoid any influence of hydrodynamic forces on cell mechanics. Beads wandered freely about the flow cell and came occasionally into contact with a HUVEC, which then started the process of endocytosis. It should be noted that due to the rather large channel cross-section and the low density of HUVECs at the channel walls, convective flow should not cause any kind of mechanical stress on the cells of the magnitude observed in the present study.

3.2.4. Measures against microbial contamination

To avoid any kind of microbial contamination during the experiments, the following measures were taken: HUVECs were cultivated in a class II biological safety laboratory according to standard protocols. For WGM experiments, glass substrate and PDMS channel were first rinsed thoroughly with acetone, ethanol, p.a. grade, and disinfected DI water, and then placed into a UV ozone cleaner (Bioforce, Nanosciences, Inc., USA) for about 2 h. Also the tubing was cleaned with copious amounts of acetone, ethanol, and desinfected DI water. This procedure was repeated after mounting of the flow cell, prior to injection of the ECGM. All aqueous solutions were made from disinfected DI water. The commercial bead suspensions were annealed in a high-pressure glass vial at 80 °C overnight prior to further use.

3.2.5. Optical set-up

For detection of the fluorescence emission of the microsphere sensors a Nikon TS100 inverted microscope was applied (Nikon Co., Tokyo, Japan). As light source a cw-HeCd laser operated at 441.6 nm (Kimmon Lasers, Tokyo, Japan) was used in order to excite WGMs from the interior of the particles upon optical pumping. As illustrated in Fig. 1b, the beam was guided via a free-beam set-up to the top of the microscope stage and then focused from above through the PDMS flow cell onto the bead by applying a quartz lens with a focal length of +75 mm. We chose not to excite the sensor from below using the microscope built-in optics to avoid unnecessary exposure of the HUVEC under study. For the same reason, the source was blocked unless needed for spectrum

acquisition. The excitation power as measured before the focusing lens was set to 10–20 μW depending on the intensity of the sensor's fluorescent emission. For the latter's spectral analysis, a monochromator (Triax 550, 600 and 2400 L/mm gratings; Horiba Jobin Yvon, Tokyo, Japan) and a cooled charge-coupled device (CCD) camera (DU440; Andor Technology, Belfast, Northern Ireland) were utilized. Scattered excitation light was separated from the fluorescence emission by means of a 2 mm Schott G475 color glass filter. To avoid any distortion of the complex process of phagocytosis, excitation power and detection settings were optimized such as to minimize total light exposure at a reasonable signal-to-noise level. CCD settings were 5 s single acquisition at 20 accumulations, yielding a total acquisition time of 100 s per spectrum. Wavelength positions of the CCD/monochromator system were calibrated by measuring a number of laser lines (HeCd at 441.60 nm, Ar Ion at 457.935, 487.9864, and 514.531 nm) and subsequent variance analysis.

3.2.6. Surface plasmon resonance (SPR)

For determination of the thickness of a potential adsorption layer formed on the sensor surface during its stabilization in the ECGM, SPR experiments were performed by means of a Biacore X instrument. Bare Biacore Au sensor chips were first cleaned in an UV ozone cleaner (BioForce Nanosciences, Inc., Ames, IA) for about 1 h for removal of air-borne organic contamination and immediately afterwards exposed to 20 mM ethanolic MUA solution for 12 min to yield a COOH-terminated gold surface. Immediately after rinsing (ethanol, DI water) and drying in a stream of nitrogen, samples were docked and primed with DI water, which was also used as rinsing buffer at a flow rate of 5 μL/min. Subsequently, thus prepared substrates were coated with two PAH/PSS double layers by injecting 60 μL of PE solution in each adsorption step, thereby mimicking the outer surface of the microsphere samples. Then, the rinsing buffer was changed to basal medium, which had been found in prior experiments to show no adsorption on the PSS-terminated surface, and full medium (basal ECGM + 10% ECGM supplement) was injected (60 μL at 5 μL/min). By four independent experiments, the mass density of the adsorption layer formed was determined to $(2.59 \pm 0.10)\ \mathrm{ng/mm^2}$. To calculate an effective layer thickness from this value, we used the well-known thickness and mass density of a monolayer of BSA (Ferrer et al., 2001), which gives a conversion ratio of $1.146\ \mathrm{ng/nm^3}$, thereby resulting in an effective thickness of the ECGM layer of (2.3 ± 0.1) nm. The use of BSA as reference protein is justified by the observation that we could not find any adsorption onto the PSS surface from the basal ECGM alone, i.e., the growth medium without growth supplement, so that most likely serum proteins, such as albumins, cause the formation of this thin adsorption layer.

4. Results and discussion

For illustration of typical bead incorporation by HUVECs, Fig. 2 displays a series of confocal transmission images of the uptake of a 6.7 μm PS particle. As detailed in Section 3.2, beads were freely floating in a microfluidic flow cell, in which HUVECs had been grown. Once a bead came into contact with a cell, in particular their microvilli, it attached and was subsequently incorporated by the cell within about 2 h from first contact. In the example of Fig. 2, the bead first contacts one microvillus, then a second one. The two microvilli start to fuse after about 20 min and the bead is pulled towards the body of the cell. Incorporation starts after about 30 min from the beginning of observation. Since the initial phase of capturing showed variation in timing, spectra recording began typically when the bead had contacted the cell body, corresponding to the 30 min state of Fig. 2.

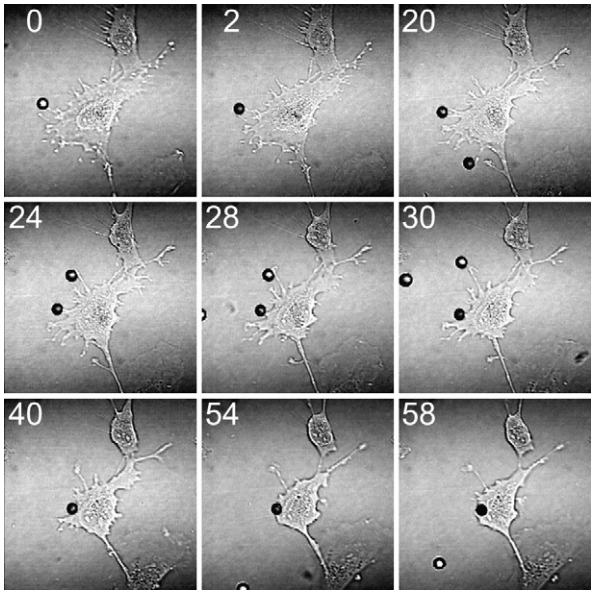

Fig. 2. Series of confocal transmission images showing the uptake of a PS bead of 6.7 μm in diameter by a surface-adhered HUVEC. The numbers give the elapsed time in minutes. In the course of time, some other beads, which are freely floating in the ECGM, are passing by. Size of picture frames: $106 \times 106\ \mu\mathrm{m}^2$.

Two sequences of WGM spectra acquired in-vitro during the endocytosis of two different beads with sizes of 7.81 μm (a) and 10.06 μm (b), respectively, are displayed in Fig. 3a and b. The peaks show up in pairs of TM/TE modes as characteristic for $q = 1$ modes in aqueous environment (Pang et al., 2008). In Fig. 3a, at $t = 0$, the peaks exhibit a small asymmetry indicating that the bead is already in contact with the HUVEC and thus experiences a heterogeneous environment. After 5 min, they exhibit a strong broadening into bands of modes, which decays during the further process of incorporation. After 106 min, finally, the peaks are highly symmetric, indicating that spherical symmetry of the cavity is preserved and thus the bead has not been altered or damaged during engulfment. Further, the red-shift of the modes indicates that the bead has in fact reached the interior of the cell with its higher refractive index relative to ECGM. The asymmetry in WGM lineshape may have two causes. First, the bead experiences an inhomogeneous environment; second, it may be elastically deformed (*cf.* Fig. 1d). In both cases degeneracy of the polar modes is lifted. Deformation of the sphere into an ellipsoid would cause a modal band of even intensity distribution between a minimum and maximum mode position, corresponding to the principal axes (*cf.* Fig. 1d). Due to the higher symmetry of these two extremes, their intensity might be somewhat enhanced. This situation is in fact found for the $t = 5$ min spectrum of Fig. 3a as indicated in Fig. 1c and d, which display selected WGM peaks in the corresponding sketch. Otherwise, the spectra exhibit only weak asymmetry, suggesting mainly an influence of the environment.

For quantification of the observed effects, the individual WGMs of the different spectra were first fitted by Lorentzian profiles for determination of their lower, weighted center, and upper band positions (for details, see Appendix A). From the weighted center positions, bead size and (average) refractive index of the bead's environment were then determined simultaneously by concurrent fitting of all five modes to their respective Airy approximations (*cf.* Appendix A). With thus obtained refractive indices, the principal axes of the deformed bead were calculated in a second fit to the respective lower and upper band positions. Fig. 4 displays resulting average refractive indices, bead radii (minimum, mean, maximum), and ratio of lower versus upper mode intensities as

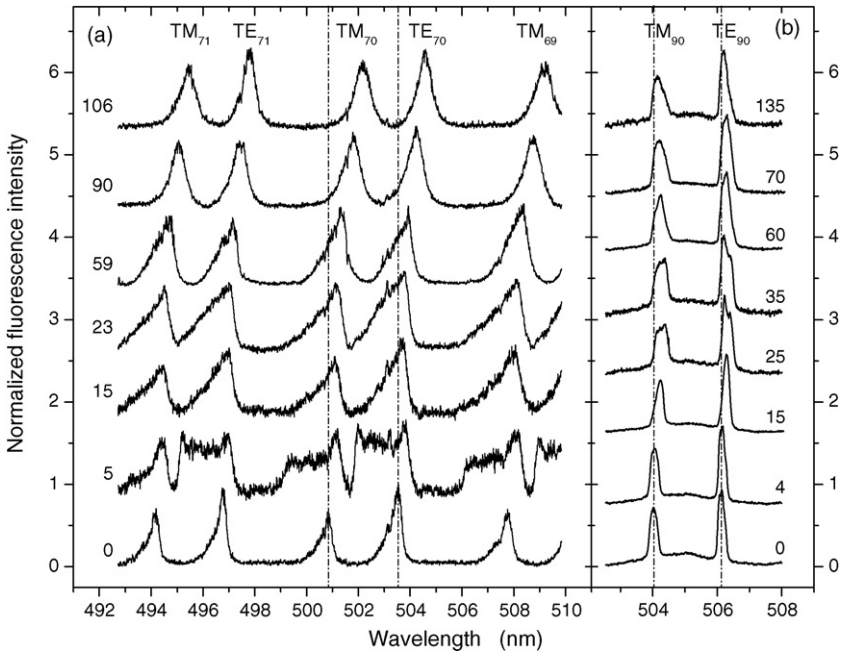

Fig. 3. Series of WGM spectra taken during the uptake of polystyrene beads of different size. (a) Successful engulfment of a bead with a diameter of 7.8 μm; (b) attempted engulfment of a bead with a diameter of 10.1 μm. In both graphs, the numbers indicate the elapsed time in minutes and the peaks are labeled according to their polarization and their mode number l as obtained from the fitting (cf. Appendix A). Spectra vertically displaced for clarity.

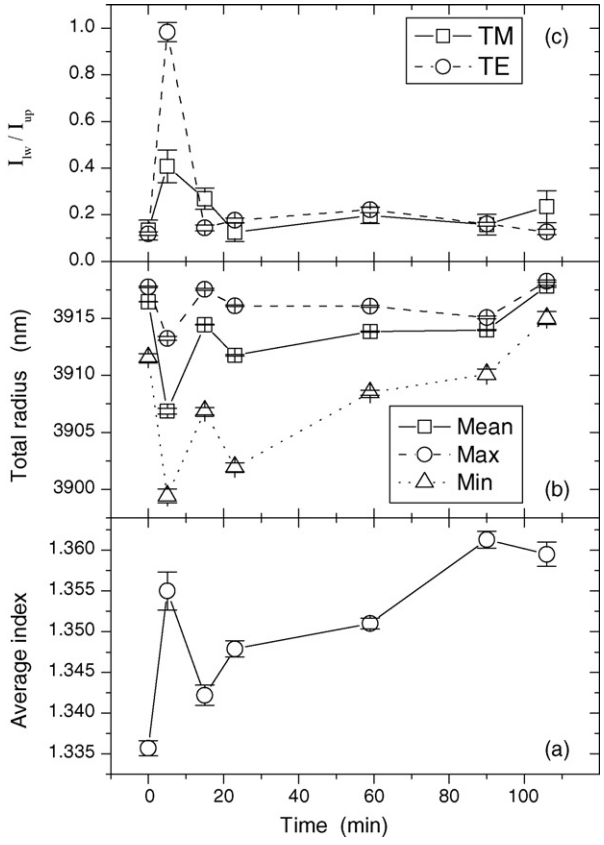

Fig. 4. Results of the quantitative evaluation of the spectra of Fig. 3a as detailed in Appendix A. (a) Average refractive index experienced by the bead in the course of its penetration into the cell; (b) average, minimum, and maximum total radii (bead radii + adsorption layer) of the deformed bead in the course of time as obtained from the WGM analysis; (c) intensity ratio, I_{lw}/I_{up}, of the Lorentzian profiles that correspond to minimum and maximum radii, i.e., those fitted to the lower (I_{lw}) and upper (I_{up}) flanks of the WGM bands. Shown is the average over all those ratios within one spectrum, i.e., over all five WGM bands, thereby yielding the statistical standard deviation indicated.

experienced by the bead during incorporation. The refractive index shows a continuous rise, indicating progressive bead engulfment, and saturates around 1.36 in good agreement with literature values for intracellular refractive indices, which are in the range of 1.36–1.38 (Curl et al., 2005; Rappaz et al., 2005). Only the value at 5 min is an exception from the monotone behavior, thus indicating that a second mechanism is dominant here, which is supposedly related to bead deformation. Fig. 4c plots the intensity ratios of lower to upper band positions for the spectra of Fig. 3a. Obviously, the ratio is small except for the 5 min spectrum, thereby giving evidence that it is mainly influenced by bead deformation and thus mechanical forces exerted by the cell. This compression is further indicated in Fig. 4b, which displays the evolution of the bead radii. Obviously, at 5 min, the bead size is smaller than otherwise.

On basis of these observations, the stress exerted by the cell is calculated by assuming that the bead is deformed into an ellipsoid, i.e., that the stress within the plane of the membrane is uniform, $\sigma_i = \sigma_{22} = \sigma_{33}$, and that the in-plane and out-of-plane strains, $\varepsilon_i = (R_i - R)/R$ and $\varepsilon_o = (R_o - R)/R$, caused by in-plane and out-of-plane stresses, σ_i and σ_o, respectively, can be calculated from minimum, R_i, average, R, and maximum, R_o, bead radii (*cf.* Appendix A). This model is in concordance with the work of Herant et al. on the mechanics of neutrophil phagocytosis (Herant et al., 2006), which gave evidence for a central pulling force along the bead's out-of-plane axis. By applying generalized Hooke's law and literature values for the material constants, in-plane and out-of-plane stress may be directly determined. However, one intricacy hampers such immediate evaluation. As can be seen from Fig. 4b, at 5 min, the bead size has shrunk in all directions, i.e., the overall bead size is reduced, thus resulting in compression, i.e., negative stress, in all directions. This, however, is an unlikely scenario, because a negative pulling force would cause bead repulsion. The reason for this discrepancy is that we neglected the thin organic layer on the bead surface, which originates from the PE coating, into which the beads had been cocooned after inking, and some protein that may have adsorbed onto it. In reference measurements applying WGM sensing (Francois and Himmelhaus, 2008) and SPR, we determined the thickness of this layer to $d = (8 \pm 1)$ nm. Since Young's mod-

Table 1
Results of spectrum analysis and stress calculation for two spectra of Fig. 3a and b.

Parameter	Unit	Spectrum	
		Fig. 3a – t = 5 min	Fig. 3b – t = 35 min
WGM fitting			
Initial total radius, r	nm	3906.86 ± 0.25	5030.06 ± 0.06
In-plane total radius, r_i	nm	3899.43 ± 0.60	5028.67 ± 0.07
Out-of-plane total radius, r_o	nm	3913.25 ± 0.18	5031.48 ± 0.07
Reference measurement			
Initial layer thickness, d	nm	8.0 ± 1.0	
Calculation based on coated-sphere model			
Initial bead radius, R	nm	3898.86 ± 1.03 (±0.25/± 1.0)	5022.06 ± 1.00 (±0.06/± 1.0)
In-plane bead radius, R_i	nm	3897.13 ± 1.13 (±0.25/± 1.10)	5021.65 ± 0.98 (±0.05/± 0.98)
Out-of-plane bead radius, R_o	nm	3901.50 ± 1.60 (±0.24/± 1.58)	5022.70 ± 1.08 (±0.05/± 1.07)
In-plane bead strain ε_i	(1e−4)	−4.43 ± 1.88 (±0.27/± 1.86)	−0.81 ± 0.32 (±0.03/± 0.31)
Out-of-plane bead strain ε_o	(1e−4)	6.77 ± 2.65 (±0.26/± 2.64)	1.29 ± 0.47 (±0.05/± 0.46)
In-plane layer thickness d_i	nm	2.30 ± 1.23 (±0.55/± 1.10)	7.02 ± 0.98 (±0.07/± 0.98)
Out-of-plane layer thickness d_o	nm	11.75 ± 1.60 (±0.27/± 1.58)	8.78 ± 1.08 (±0.07/± 1.07)
In-plane layer strain ε_i^L	(1e−1)	−7.12 ± 1.32 (±0.69/± 1.13)	−1.23 ± 0.24 (±0.09/± 0.22)
Out-of-plane layer strain ε_o^L	(1e−1)	4.68 ± 1.34 (±0.34/± 1.29)	0.97 ± 0.31 (±0.09/± 0.29)
In-plane stress $\sigma_i = \sigma_i^L$	MPa	−1.282 ± 0.593(±0.123/± 0.580)	−0.221 ± 0.096(±0.017/± 0.094)
Out-of-plane stress $\sigma_o = \sigma_o{}^L$	MPa	0.843 ± 0.279 (±0.062/± 0.272)	0.175 ± 0.056 (±0.016/± 0.054)

The upper section gives the total radii as obtained from WGM fitting, whereby the errors are calculated as ±10% variances of the respective best fit. The center section gives the adsorption layer thickness as obtained by SPR, and the third section gives the results of the stress calculation based on the coated-sphere model. In the latter section, besides the total error given, the values in parentheses refer to the errors arising from the WGM fitting (left) and those caused by the presence of the adsorption layer (right).

uli for PE and serum proteins are much smaller than that of PS, a significant deformation of this layer must be expected. Because it is very thin, $d \ll R$, it can be treated as stratified layer neglecting coupling between in-plane and out-of-plane components, d_i and d_o. Assuming $\sigma_o = \sigma_o^L$ and $\sigma_i = \sigma_i^L$, where σ_i^L and σ_o^L are in-plane and out-of-plane stress of the layer, Hooke's law can be solved for in-plane and out-of-plane strains experienced by bead and layer, respectively (for details, see Appendix A). Table 1 lists the results. The errors are separated into those caused by spectra evaluation, i.e., the WGM sensor itself, and those caused by poor knowledge of thickness and composition of the organic layer.

The errors given in Table 1 indicate that the interference-based transducer mechanism applied achieves satisfactory accuracy despite of the subtlety of the effects and that current limitations in precision are mainly due to insufficient knowledge of the bead's coating. These latter implications, however, were not the focus of this explorative study. Furthermore, even the present results give valuable insight into the mechanism of endocytosis. Both, in-plane and out-of-plane stresses are significantly larger than what could be expected from passive cortical tension alone. Assuming a minimum membrane thickness of 5 nm (Nelson and Cox, 2005), a maximum cortical tension of 1 mN/m translates into a tensile stress of 200 kPa, which is clearly outside the total error of our results, thus indicating the presence of an active force. While the in-plane stress is expected to result from a superposition of passive and active components, the out-of-plane stress may be solely attributed to the pulling force. With an average diameter of 7.8 μm, the total force onto the projected bead area in out-of-plane direction amounts to 40.2 μN. This large value cannot be explained solely by the presence of surface molecular motors as postulated by Herant et al. (Herant et al., 2006). Little is known about the density of surface molecular motors, but a reasonable upper limit – from experimental evidence (Herant et al., 2006) as well as simple steric considerations – seems to be ∼1000 motors/μm^2. Given a maximum force per motor (Micoulet et al., 2005) of 1 pN this results in 95 nN total force. Therefore, either our stress estimates are false by an unlikely factor of ∼420 or another way of force generation is present. An error discussion is given in Appendix A. As alternative mechanism we conceive that a major part of the cytoskeleton in vicinity of the bead, which comprises a dense network of different kinds of filaments and molecular motors, acts on the bead as a whole. While the details of such "global" cortex action need further clarification, we can at least estimate whether such large force is in general compliance with the cell's power balance. The 7.8 μm bead studied is moved by the cell within 106 min from the outside to the inside for a distance of ∼10 μm. Thus, the work performed by the cell amounts to ∼400 pJ, the power consumption to ∼63 fW, resulting in a consumption rate of 1.6×10^6 ATP/s (Micoulet et al., 2005). The total ATP production rate within a cell is about 10^{10} ATP/s (Micoulet et al., 2005), so that the internalization of the bead requires only a small fraction of 0.016% of the cell's power balance.

Further evidence for a global cortex action can be gained from the spectra of Fig. 3b, which show a bead of 10.1 μm diameter in contact with a HUVEC. In this case, the bead is too large for endocytosis. After an initial peak shift indicating that the bead has approached the cell, mode broadening is observable similar to that of Fig. 3a.[3] However, this time it continues to remain for over 30 min. Then, the cell seems to release the bead as evident from the WGMs' blue shift towards to their initial values. The stress calculation gives a 5–6-fold smaller stress compared with the first bead (Table 1). This is counterintuitive if the force arises solely from surface-bound molecular machinery, since a larger bead bears more surface area. For a force exerted by the entire cortex, however, it is reasonable that a bead, which penetrates to lesser extent into the cortex, experiences a smaller force, i.e., the cortex cannot fully grab the bead. This might be understood as a kind of "pincer movement" of simultaneous pulling and squeezing, since both in-plane and out-of-plane stress components are of similar magnitude within a difference roughly of the order of the maximum passive stress component of some hundreds of kPa. Such combined action of the cortical apparatus appears not implausible, since the cell might try to reduce the bead diameter to minimize its efforts.

5. Conclusions

More work is needed to elucidate the role of the cortex during endocytosis in all detail. It has been the goal of the present

[3] Please note that due to the smaller free spectral range of a larger bead, i.e., a smaller mode spacing, the observed spectral shifts are smaller for same changes in the beads' environment.

work, however, to introduce a new method of biomechanical sensing of live cells and to demonstrate its feasibility rather than to clarify all aspects of the complex process of endocytosis. Presently, the errors in the results are mainly caused by poor knowledge of material constants rather than the transducer mechanism itself. Therefore, the overall precision of the method may be improved soon. Another factor of uncertainty is related to the unknown composition of the thin adsorption layer forming on the beads during their stabilization in ECGM. Here, future work will aim at finding conditions avoiding such adsorption layer to facilitate specific functionalization, thereby opening the entire repertoire of biochemical signaling proteins to a novel kind of biomechanical studies.

Another aspect of our work is related to the size limit for particle uptake by HUVECs, which we found to be around 8 μm. While it is known that some cell types may incorporate particles up to 10 μm in diameter (Herant et al., 2006; Kodali et al., 2007), a previous study on PS bead uptake by HUVECs had found an upper size limit of about 500 nm (Wiewrodt et al., 2002). In that case, however, the particle surface had been specifically functionalized with platelet endothelial cell adhesion molecules, which may favor internalization via a specific pathway, such as clathrin-mediated endocytosis. In our case, however, the particle surface was coated with a thin layer of growth medium constituents, which might leave freedom also for other mechanisms. Obviously, incorporation of particles of several micrometers in size requires a reconfiguration of the actin network and – as found here – an active pulling force by the cytoskeleton, which cannot be explained by a clathrin-mediated pathway of internalization.

In summary, we have shown that by applying internal WGM excitation in fluorescent microparticles, WGMs can be generated in three dimensions in particles sufficiently small for their endocytosis by live cells. In addition, WGMs may be excited and detected optically, thus facilitating the undistorted observation of mechanical deformations of the probe during its endocytosis. Our analysis of the particle's deformation reveals a recently postulated active stress component induced by the cytoskeletal machinery with a magnitude of up to five times that of the passive cortical tension. Further, we could validate that the size limit for endocytosis of probe particles by HUVECs lies at about 8 μm and thus in the typical size range of leukocytes, thereby putting a new angle on the transcellular migration pathway of the inflammatory response. While leukocyte-endothelial cell interaction is expectedly a highly complex mutual biochemical and biomechanical process of two living organisms, substitution of one of them by an artificial particle may open the opportunity to study the role of the two partners separately from each other. In other areas of immunology, for example in the phagocytosis of macrophages or other professional phagocytes, the use of these sensor particles as model phagosomes may open a more direct and unveiled access to the biomechanical forces involved, in particular because the transducer mechanism is hidden inside the probe and therefore is not recognized by the phagocyte. Also, any conditioning of the phagocyte, such as its fixation, which is required, e.g., in aspiration techniques, is not needed. In cancer research, where it has been found that the biomechanical properties of the cytoskeleton of cancer cells defer significantly from those of non-malignant cells (*cf.*, e.g., Brunner et al., 2009, and references therein), an easily applicable, microscopic non-destructive probe for cytoskeletal stress may be of interest not only for basic studies, but also even for initial diagnosis.

Altogether, it is therefore our hope that the new method presented here as well as the primary findings obtained will stimulate workers in such different fields as optical (bio-)sensing, remote sensing, cell biology, inflammation and immunology, and cancer research.

Acknowledgement

The authors are indebted to T. Fujii and S. Spratt for HUVEC culturing and to S. Spratt for acquisition of the confocal transmission images.

Appendix A. Evaluation of WGM spectra

The evaluation of the WGM series proceeded in four steps. First, the individual WGM peaks were fitted by a number of Lorentzian profiles to determine their exact wavelength positions and widths. Subsequently, these results were used for fitting of the average refractive index experienced by the sensor in the different steps of bead incorporation. Then, using the average index, in-plane and out-of-plane radii were determined and subsequently used for strain and stress calculations.

A.1. WGM fitting

To allow a numerical analysis of the spectra measured, the precise peak positions must be known. Their determination, however, is hampered by the fact that the WGMs show a significant asymmetry and broadening during the process of endocytosis, indicating a lifting of the degeneracy of the modes with respect to their polar orientation, i.e., in the quantum number m (*cf.* Fig. 1c and d). Most importantly, besides determination of the average peak position, the shortest and longest wavelength contribution to each peak needs to be known, because this total extension of the mode allows calculation of minimum and maximum bead radii in the corresponding stage of uptake and thus comprises information about the mechanical stress exerted by the cellular cortex onto the bead. Therefore, the individual WGMs of the different spectra shown in Fig. 3a and b were fitted by a number of Lorentzian profiles using the peak fitting module of origin 7.5Pro. We neglected inhomogeneous peak broadening (as e.g. implemented by the use of Voigt profiles) because the cavities were operated below lasing threshold and thus their spectral characteristics should be dominated by homogeneous broadening. Further, it was desirable to keep the number of free parameters as small as possible and finally, trials with Voigt profiles gave basically the same results in view of mode positions. The most important question to answer was then how many individual Lorentzian profiles can be reasonably distinguished within a single mode. From a theoretical viewpoint, lifting the degeneracy in m gives rise to $2\ell + 1$ different modes. As will be shown below, for the spectra shown in Fig. 3a, ℓ has been determined to 70, thus yielding a total of 141 individual profiles within a single peak. From a practical viewpoint, using such a large number of profiles for the description of a WGM of few nanometers in bandwidth would be obviously overdoing it, in particular because the WGMs show a finite bandwidth even in the symmetric case (*cf.*, e.g., 106 min spectrum in Fig. 3a). To find a reasonable description, we therefore proceeded as follows. Some information about the bandwidth of the individual profiles within a single WGM can be obtained from the steepness of its flanks. For symmetry reasons, the profiles with lowest and highest peak position should have similar bandwidths (*cf.* Fig. 1c and d). Therefore, the individual WGMs within the same spectrum were fitted with an increasing number of Lorentzian profiles until the steep flanks of the bands were described well. Thereby, we tried two different approaches. In the first one, only the smallest and highest profile within a WGM shared their bandwidths during the fit, in the second case, all profiles shared the same width. While the former approach reflects the fact that the two extreme cases, i.e., the WGMs traveling along the minor and major axes of the ellipsoid, should show somewhat lower losses because of their higher symmetry as com-

pared to WGMs traveling off these main symmetry axes, the second approach removes some arbitrariness from the description of these low symmetry modes. A careful comparison of the results did not give any difference in the further evaluation and we decided to use the second set of data with all bandwidths shared.

Summarizing, the WGMs were fitted by using a number of Lorentzian profiles with shared bandwidths, whereby the number of profiles was determined as the minimum number of profiles needed to describe the flanks of the WGMs well. This number was fixed for each individual spectrum and kept constant for all WGMs within this spectrum.

A.2. Determination of bead parameters

From the results obtained by peak fitting, the average refractive index and average, minimum, and maximum bead radii were determined as follows. In a first step, the average position of each mode i of a spectrum was calculated as weighted average by $\bar{\lambda}_i = \sum_j c_j^i \lambda_j^i / \sum_j c_j^i$, where c_j^i is the amplitude of Lorentzian profile j with peak position λ_j^i used to fit mode i. These average mode positions were then used to determine average bead radius and average refractive index of the bead's environment simultaneously by fitting of WGM Airy approximations to the average mode positions. Useful descriptions of Airy approximations for particles in a dielectric environment have been recently derived (Pang et al., 2008). These formulas are easier to deal with numerically than the exact solutions (Oraevsky, 2002) and yield good agreement in the particle size range we are applying here (Pang et al., 2008; Francois and Himmelhaus, submitted for publication). For fitting, which was programmed in *matlab R2007a*, the total deviation between measured and calculated mode positions, given as

$$\Delta = \sum_i \mathrm{abs}(\bar{\lambda}_i - \lambda(p, q, \ell, R, n_\mathrm{s}, n_\mathrm{e})), \tag{A1}$$

was minimized by variation of all relevant parameters, i.e., mode number, bead radius, and refractive index, until sufficient precision was reached (three decimal places for radii, five decimal places for refractive indices). In Eq. (A1), λ refers to the mode position calculated via the Airy approximation, p is its state of polarization (p = TE or TM), q and ℓ are WGM mode order and mode number, respectively, R is the bead radius, n_s its refractive index (n_s = 1.5590 for dye-doped polystyrene microbeads, for details see Francois and Himmelhaus, submitted for publication), and n_e the refractive index of the bead's environment.

Subsequently, thus determined refractive indices were kept fixed and minimum and maximum bead radii, corresponding to the main symmetry axes of the ellipsoid, were calculated from the corresponding minimum and maximum mode positions, respectively. These are the results shown in Fig. 4. The spectra in Fig. 3b were treated analogously.

The only uncertainty introduced in this procedure was that we had to decide a priori which of the WGMs in a spectrum correspond to TM and which comprise TE modes. Further, we assumed that all of the modes observed are of 1st order, i.e., q = 1. Both of these assumptions were made based on the literature (Zijlstra et al., 2007; Pang et al., 2008; Francois et al., 2008) and the observations made by applying the Airy approximations to different environmental refractive indices. For indices in the range of 1.3–1.4, it can be seen that TM and TE modes of same mode number form pairs, i.e., have a smaller distance to each other than to modes with differing mode number, irrespective of the polarization of the latter. Therefore, a close look at the spectra given in Fig. 3a shows that we are dealing with 2.5 pairs here. The simulation using the Airy approximations also illustrates that within a pair the TM mode is the peak at lower wavelength. Further, it is known from the literature that TM modes typically comprise broader bandwidths than TE modes (Zijlstra et al., 2007; Francois and Himmelhaus, 2009), which is also in agreement with the spectra of Fig. 3. Therefore, summarizing, the spectra in Fig. 3a show three TM and two TE modes, the mode numbers of which have to be determined by applying the fitting procedure described above. Accordingly, Eq. (A1) can be rewritten as

$$\begin{aligned}\Delta_{\mathrm{Fig.3a}} = {} & \mathrm{abs}(\lambda_1 - \lambda(TM, q = 1, \ell, R, n_\mathrm{s}, n_\mathrm{e})) \\ & + \mathrm{abs}(\lambda_2 - \lambda(\mathrm{TE}, q = 1, \ell, R, n_\mathrm{s}, n_\mathrm{e})) \\ & + \mathrm{abs}(\lambda_3 - \lambda(\mathrm{TM}, q = 1, \ell - 1, R, n_\mathrm{s}, n_\mathrm{e})) \\ & + \mathrm{abs}(\lambda_4 - \lambda(\mathrm{TE,q} = 1, \ell - 1, R, n_\mathrm{s}, n_\mathrm{e})) \\ & + \mathrm{abs}(\lambda_5 - \lambda(\mathrm{TM}, q = 1, \ell - 2, R, n_\mathrm{s}, n_\mathrm{e}))\end{aligned} \tag{A2}$$

with the experimentally determined WGM positions $\lambda_i < \lambda_{i+1}$.

A.3. Calculation of mechanical stress

For the calculation of the stress exerted by the cell onto the bead, Hooke's generalized law for isotropic media was applied (Symon, 1971):

$$\begin{bmatrix}\sigma_{11}\\ \sigma_{22}\\ \sigma_{33}\\ \sigma_{23}\\ \sigma_{13}\\ \sigma_{12}\end{bmatrix} = \frac{E}{(1+\nu)(1-2\nu)} \times \begin{bmatrix} 1-\nu & \nu & \nu & 0 & 0 & 0 \\ \nu & 1-\nu & \nu & 0 & 0 & 0 \\ \nu & \nu & 1-\nu & 0 & 0 & 0 \\ 0 & 0 & 0 & \frac{1-2\nu}{2} & 0 & 0 \\ 0 & 0 & 0 & 0 & \frac{1-2\nu}{2} & 0 \\ 0 & 0 & 0 & 0 & 0 & \frac{1-2\nu}{2} \end{bmatrix} \begin{bmatrix}\varepsilon_{11}\\ \varepsilon_{22}\\ \varepsilon_{33}\\ \varepsilon_{23}\\ \varepsilon_{13}\\ \varepsilon_{12}\end{bmatrix} \tag{A3}$$

Here, σ is the stress inducing the strain ε as mediated by Young's modulus E. The ratio ν of out-of-plane strain (perpendicular to the applied load) to in-plane strain (in the direction of the applied load),

$$\nu = -\frac{\varepsilon_\mathrm{o}}{\varepsilon_\mathrm{i}}, \tag{A4}$$

is called "Poisson coefficient" or "Poisson's ratio" and is a property of the respective material. It states basically that strain induced in one direction will create strain also in perpendicular direction, thereby causing a coupling of the different tensor elements.

We assume that the deformation of the bead is symmetric in the plane of the cell membrane and that it is this plane, which is related to the minimum diameter of the spheroid, i.e., $\varepsilon_\mathrm{i} = \varepsilon_{22} = \varepsilon_{33}$, whereas the strain perpendicular to this plane is $\varepsilon_\mathrm{o} = \varepsilon_{11}$ and therefore $\sigma_{22} = \sigma_{33} = \sigma_\mathrm{i}$ (stress applied by the cell onto the bead), $\sigma_{11} = \sigma_\mathrm{o}$ (see Fig. 1d for definition of coordinate system and in-plane/out-of-plane orientations). With these assumptions, Eq. (A3) can be rewritten as

$$\begin{aligned}\sigma_\mathrm{o} &= \frac{E}{(1+\nu)(1-2\nu)}[(1-\nu)\varepsilon_\mathrm{o} + 2\nu\varepsilon_\mathrm{i}] \\ \sigma_i &= \frac{E}{(1+\nu)(1-2\nu)}[\varepsilon_\mathrm{i} + \nu\varepsilon_\mathrm{o}]\end{aligned} \tag{A5}$$

to obtain the in-plane and out-of-plane stress components σ_i and σ_o.

Eq. (A5) does not account for the presence of the thin surface layer on the bead arising from the PE coating and an additional layer that adsorbed onto the PE during the stabilization phase in ECGM. Such layer is crucial because it supposedly comprises a much smaller Young's modulus and thus exhibits a larger compression during the bead uptake. In fact we found that direct application of Eq. (A5) for calculation of the stress components leads to negative stress in both directions, i.e., in-plane and out-of-plane. In such case, however, the bead would not be pulled into the cell, but the forces would move it out. This obvious contradiction to the observations is resolved when the thin adsorption layer is taken into account as we will show in the following.

Based on previous work (Francois and Himmelhaus, 2008) and the SPR study described in Section 2, we determined the thickness of the PE layer to (5.7 ± 0.82) nm and that arising from the growth medium to (2.3 ± 0.10) nm, yielding a total thickness of $d = (8.0 \pm 1.0)$ nm. The composition of the ECGM layer is unknown but seems to arise from proteins present in the ECGM supplement. Since proteins in question, such as serum albumin, show significantly higher Young's moduli (Ahluwalia et al., 1996; Brownsey et al., 2003) than the PE layer (Mermut et al., 2003), we decided to treat the adsorption layer as a single layer with the elastic properties of the PE film as the worst case estimate.

The thickness of the soft adsorption layer is much smaller than the bead radius, i.e., $d_L \ll R$, so that coupling between in-plane and out-of-plane components of this layer is not expected. Therefore, we can treat the two directions independently of each other and use an isotropic Hooke's law for their stress–strain relation

$$\sigma_i^L = E_L \varepsilon_i^L \quad \text{and} \quad \sigma_o^L = E_L \varepsilon_o^L, \tag{A6}$$

where σ_i^L and σ_o^L are the stress exerted on the layer in in-plane and out-of-plane directions, respectively, E_L is Young's modulus of the layer, and ε_i^L and ε_o^L are the respective strain components. The stress experienced by bead and adsorption layer in the two principal directions must be the same, i.e.,

$$\sigma_i = \sigma_i^L \quad \text{and} \quad \sigma_o = \sigma_o^L. \tag{A7}$$

Further, the deformation measured by means of the WGM transducer mechanism must be interpreted as total deformation of bead and adsorption layer, i.e.,

$$r = R + d, \quad r_i = R_i + d_i, \quad \text{and} \quad r_o = R_o + d_o, \tag{A8}$$

where variables without index refer to the initial, i.e., stress-free, state prior to bead uptake, index "i" assigns the in-plane variables and index "o" out-of-plane variables, and variables r_x refer to measured total radii, R_x to bead radii, and d_x to corresponding layer thicknesses.

Finally, the in-plane and out-of-plane strain components are given as

$$\varepsilon_i = \frac{R_i - R}{R}, \quad \varepsilon_i^L = \frac{d_i - d}{d}, \quad \varepsilon_o = \frac{R_o - R}{R}, \quad \varepsilon_o^L = \frac{d_o - d}{d}, \tag{A9}$$

where the indexing is analogous to that used above. By inserting Eqs. (A5) and (A6) into (A7) and applying Eqs. (A8) and (A9), (A5) can be solved for R_i and R_o as a function of measured quantities only, i.e., R, d, and materials constants. Then, d_i and d_o can be determined via Eq. (A8). These are the results given in the third section from top of Table 1.

A.4. Error calculation

In the following, the error calculation applied to the different steps of data analysis will be reviewed. Peak fitting of the WGMs let typically to deviations of $\delta\lambda < 0.006$ nm for the high wavelength limit and $\delta\lambda < 0.03$ nm for the low wavelength limit. The difference arises from the fact that the high wavelength limit of the WGMs is typically better defined due to the higher steepness of the respective flanks. One exception is the 5 min spectrum of Fig. 3a, which shows and almost even intensity distribution throughout the WGM bands. Accordingly, the errors given by the fitting routine as variances of the mean values were typically <0.01 nm for both, low and high wavelength limits of the WGM bands. In any case, these errors are much smaller than those introduced during the subsequent evaluation and therefore could be neglected.

The fitting of bead radii and refractive indices according to Eq. (A1) resulted in surprisingly small values for the total deviation Δ (*cf.* Eq. (A1)), which was typically smaller than 0.1 nm, i.e., 0.02 nm per individual peak. This good agreement, which is basically of the same order as the errors introduced by the peak fitting, underlines the accuracy of the Airy approximations in the particle size range used here. A direct error calculation therefore would have involved the independent variation of all different peaks according to their errors obtained by the peak fitting routine. This, however, seemed too tedious. Therefore, by sacrificing some precision, the different parameters were varied independently of each other such that the minimum deviation Δ achieved for the best fit was raised by 10% of its respective minimum value, i.e., $(\Delta_{\pm\text{boundary}} - \Delta_{\min})/\Delta_{\min} \stackrel{!}{=} 0.1$. These $\pm 10\%$ Δ boundaries are the errors given for the results of Fig. 4 as well as the parameters listed in the "WGM fitting" section of Table 1. Errors of experimental values, such as layer thicknesses, etc., were calculated as standard deviations from the mean.

For determination of the errors of the strain and stress parameters according to above described model, the different input variables were varied independently according to their respective errors to give the resulting deviation of the dependent quantity, such as listed in the "Calculation based on coated-sphere model" section of Table 1. Thereby, the errors of the input parameters were the $\pm 10\%\Delta$ boundaries for fitted radii and refractive indices as described above, experimental errors as determined by SPR and prior work (Francois and Himmelhaus, 2008) for the thickness of the adsorption layer, and errors taken from the literature for materials constants. From these individual errors, the total errors were calculated by means of Gaussian error propagation. In Table 1, besides these total errors, also the errors resultant from the WGM fitting alone and those introduced by the presence of the adsorption layer are given. The latter comprises the experimental error in determining the layer thickness as well as those introduced by poorly known materials constants, such as the layer's Young's modulus. For Young's modulus of the PS beads we used a value of $E = 2.55$ GPa (Heim et al., 2002). Since the bead is much stiffer than the soft adsorption layer, a variation of this value led only to small changes in the results and thus could be neglected.

Summarizing, the materials constants were used as follows:

Refractive index of polystyrene (Francois and Himmelhaus, submitted for publication)*:* 1.5590.
Young's modulus of polystyrene (Heim et al., 2002)*:* 2.55 GPa.
Poisson's ratio of polystyrene (Seitz, 1993)*:* 0.354.
Young's modulus of PE layers (Mermut et al., 2003)*:* (1.8 ± 1) MPa at pH 7.

References

Ahluwalia, A., Stussi, E., Domenici, C., 1996. Langmuir 12, 416–422.
Apodaca, G., 2001. Traffic 2, 149–159.
Brownsey, G.J., Noel, T.R., Parker, R., Ring, S.G., 2003. Biophys. J. 85, 3943–3950.
Brunner, C., Niendorf, A., Käs, J.A., 2009. Soft Matter 5, 2171–2178.
Caruso, F., Lichtenfeld, H., Donath, E., Möhwald, H., 1999. Macromolecules 32, 2317–2328.
Cinamon, G., Shinder, V., Alon, R., 2001. Nat. Immunol. 2, 515–522.
Cook-Mills, J.M., Deem, T.L., 2005. J. Leukoc. Biol. 77, 487–495.

Curl, C.L., Bellair, C.J., Harris, T., Allman, B.E., Harris, P.J., Stewart, A.G., Roberts, A., Nugent, K.A., Delbridge, L.M.D., 2005. Cytometry A 65, 88–92.
Feng, D., Navy, J.A., Pyne, K., Dvorak, H.F., Dvorak, A.M., 1998. J. Exp. Med. 187, 903–915.
Ferrer, M.L., Duchowicz, R., Carrasco, B., de la Torre, J.G.A., Acuña, A.U., 2001. Biophys. J. 80, 2422–2430.
Francois, A., Himmelhaus, M., 2008. Appl. Phys. Lett. 92, 141107/1-3.
Francois, A., Himmelhaus, M., 2009. Appl. Phys. Lett. 94, 031101/1-3.
Francois, A., Himmelhaus, M., 2009. Sensors, submitted for publication.
Francois, A., Krishnamoorthy, S., Himmelhaus, M., 2008. Proc. SPIE 6862, 68620Q/1-8.
Garcia, J.G.N., Verin, A.D., Herenyiova, M., English, D., 1998. J. Appl. Physiol. 84, 1817–1821.
Gerlach, M., Rakovich, Y.P., Donegan, J.F., 2007. Opt. Express 15, 3597–3606.
Greenberg, S., 2001. J. Cell Sci. 114, 1039–1040.
Heim, L.O., Ecke, S., Preuss, M., Butt, H.-J., 2002. J. Adhes. Sci. Technol. 16, 829–843.
Herant, M., Heinrich, V., Dembo, M., 2005. J. Cell Sci. 118, 1789–1797.
Herant, M., Heinrich, V., Dembo, M., 2006. J. Cell Sci. 119, 1903–1913.
Hess, K.L., Tudor, K.S., Johnson, J.D., Osati-Ashtiani, F., Askew, D.S., Cook-Mills, J.M., 1997. Exp. Cell Res. 236, 404–411.
Hordijk, P.L., 2006. FEBS J. 273, 4408–4415.
Ilchenko, V.S., Volikov, P.S., Velichansky, V.L., Treussart, F., Lefèvre-Seguin, V., Raimond, J.-M., Haroche, S., 1998. Opt. Commun. 145, 86–90.
Kielbassa, K., Schmitz, C., Gerke, V., 1998. Exp. Cell Res. 243, 129–141.
Kippenberg, T.J., Rokhsari, H., Carmon, T., Scherer, A., Vahala, K.J., 2005. Phys. Rev. Lett. 95, 033901/1-4.
Kirsch, T., Woywodt, A., Beese, M., Wyss, K., Park, J.-K., Erdbruegger, U., Hertel, B., Haller, H., Haubitz, M., 2007. Blood 109, 2854–2862.
Kodali, V.K., Roos, W., Spatz, J.P., Curtis, J.E., 2007. Soft Matter 3, 337–348.
Kuwata-Gonokami, M., Takeda, K., Yasuda, H., Ema, K., 1992. Jpn. J. Appl. Phys. 31, L99–L101.
Lösche, M., Schmitt, J., Decher, G., Bouwman, W.G., Kjaer, K., 1998. Macromolecules 31, 8893–8906.
Matsko, A.B., Ilchenko, V.S., 2006. IEEE J. Sel. Top. Quant. Electron. 12, 3–14.
Mermut, O., Lefebvre, J., Gray, D.G., Barrett, C.J., 2003. Macromolecules 36, 8819–8824.
Micoulet, A., Spatz, J.P., Ott, A., 2005. Chem. Phys. Chem. 6, 663–670.
Nelson, D.L., Cox, M.M., 2005. Lehninger—Principles of Biochemistry, 4th ed. W. H. Freeman and Co, New York, p. 369 (Figure 11-1).
Oraevsky, A.N., 2002. Quant. Electron. 32, 377–400.
Pang, S., Beckham, R.E., Meissner, K.E., 2008. Appl. Phys. Lett. 92, 221108/1-3.
Porta, C., James, P.S., Phillips, A.D., Savidge, T.C., Smith, M.W., Cremaschi, D., 1992. Exp. Physiol. 77, 929–932.
Rabinovitch, M., 1995. Trends Cell Biol. 5, 85–87.
Rappaz, B., Marquet, P., Cuche, E., Emery, Y., Depeursinge, C., Magistretti, P.J., 2005. Opt. Express 13, 9361–9373.
Remmerbach, T.W., Wottowah, F., Dietrich, J., Lincoln, B., Wittekind, C., Guck, J., 2009. Cancer Res. 69, 1728–1732.
Seitz, J.T., 1993. J. Appl. Polym. Sci. 49, 1331–1351.
Serpengüzel, A., Arnold, S., Griffel, G., 1995. Opt. Lett. 20, 654–656.
Symon, K.R., 1971. Mechanics, third ed. Addison-Wesley, Reading, MA.
Vahala, K.J., 2003. Nature 424, 839–846.
Vestweber, D., 2007. Immunol. Rev. 218, 178–196.
Vollmer, F., Arnold, S., 2008. Nat. Methods 5, 591–596.
Weller, A., Liu, F.C., Dahint, R., Himmelhaus, M., 2008. Appl. Phys. B 90, 561–567.
Wiewrodt, R., Thomas, A.P., Cipelletti, L., Christofidou-Solomidou, M., Weitz, D.A., Feinstein, S.I., Schaffer, D., Albelda, S.M., Koval, M., Muzykantov, V.R., 2002. Blood - Hemost. Thromb. Vasc. Biol. 99, 912–922.
Wolfe, J., Dowgert, M.F., Steponkus, P.L., 1986. J. Membr. Biol. 93, 63–74.
Zijlstra, P., van der Molen, K.L., Mosk, A.P., 2007. Appl. Phys. Lett. 90, 161101/1-3.